

RESEARCH ARTICLE

Enhance Low Visibility Image Using Haze-Removal Framework

PING JUEI LIU 

Department of Artificial Intelligence and Computer Engineering, National Chin-Yi University of Technology, Taichung 411030, Taiwan

e-mail: immich0716@gmail.com

ABSTRACT We proposed a novel image enhancement framework to raise the visibility of the image's content. Our primary concern is eliminating haze-like effects and simultaneously increasing images' brightness. Dehazing and luminance enhancement algorithms are considered standard techniques to overcome these issues. However, natural environments usually involve several unfavorable conditions simultaneously, such as insufficient illumination, blur caused by the haze, and color cast resulting from the sun or scattering; this makes dehazing algorithms challenging to overcome environmental issues. Besides, dehazing algorithms sometimes result in artifacts. The proposed framework solves these issues simultaneously by implementing a double-side enhancement in contrast and brightness based on a new dehazing algorithm. We compare the new dehazing algorithm with others using full-reference benchmarks to ensure performance stability. Afterward, to show the advantage of using the new dehazing algorithm, we evaluate the compatibility between the proposed framework and all dehazing algorithms using non-reference benchmarks. At last, we pair dehazing and luminance enhancement algorithms and compare the combinations with the proposed framework. Eventually, experimental results prove that the new dehazing algorithm outperforms others and is better compatible with the proposed framework. Meanwhile, the proposed framework is superior in contrast and brightness enhancements and outperforms the single dehazing algorithm or the combinations.


INDEX TERMS Image enhancement, contrast enhancement, brightness enhancement, low-visibility image, haze removal, dehaze, fog.

I. INTRODUCTION

Image clarity was usually interfered with by haze, fog, smoke, rain, and unideal illumination. Some of the above phenomena resulted in haze-like effects and degraded visibility. These natural phenomena were all related to the atmospheric impacts caused by the scattering, and dehazing algorithms [1], [2], [3], [4], [5], [6], [7], [8], [9], [10], [11], [12] were the standard techniques to eliminate scattering effects. The early design of dehazing algorithms focused on visibility enhancement or haze-pattern analysis rather than scene restoration [1], [2], [3], [4]. Researchers used an atmospheric model that obeyed Koschmieder's Law [1], assuming the scene was composed of the global atmospheric light and actual scene radiance; accordingly, the atmospheric model helped eliminate haze-like effects. After that,

machine-learning-based methods became the mainstream of dehazing study. Some research [5], [6], [7], [8] still followed Koschmieder's Law; others [9], [10], [11], [12], [13] generated a clear image directly with the help of deep-learning networks learned from hazy datasets. In this stage, dehazing algorithms were commonly known as the image restoration algorithm; thus, visibility enhancement was only a part of the goals for dehazing algorithms, and full-reference benchmarks [14], [15] became the most important standards to evaluate the performance [4], [5], [6], [7], [8], [9], [10], [11], [12], [13].

Nevertheless, from the perspectives of applications, dehazing algorithms were usually considered the image enhancement method to improve the clarity or quality of unfavorable images, as reported in [16]. Sometimes, applications also wished that dehazing algorithms could improve recognition accuracy. As a significant trend, more and more researchers evaluated the dehazing algorithm using non-reference

The associate editor coordinating the review of this manuscript and approving it for publication was Sudhakar Radhakrishnan .

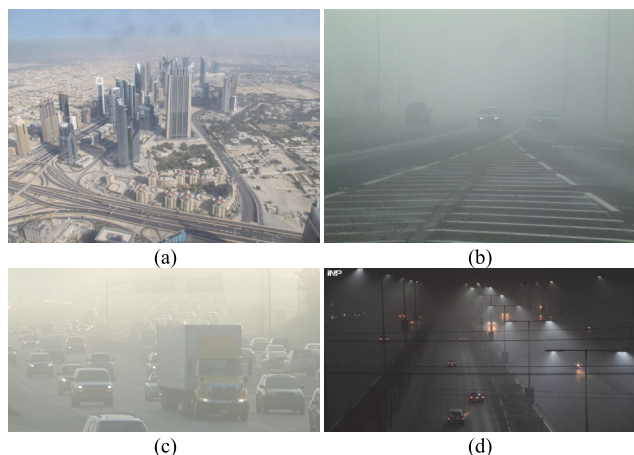


FIGURE 1. Low visibility images caused by haze (a) during the day in a high-light environment, (b) during the day in a low-lowlight environment, (c) in the evening, and (d) at night.

benchmarks [17], [18], [19], which assessed the naturalness, contrast, and brightness of images. As the pre-processing algorithms, they played important roles in various fields, such as semantic segmentation [20], object recognition [21], [22], security sensor applications [23], airport control [24], and auto-pilot [20], [25]. However, the performance of dehazing algorithms was quite limited while dealing with various haze conditions. According to the report in [8], machine-learning-based dehazing algorithms were weak in dense haze situations, thereby unsuitable for low-visibility images. On the contrary, early dehazing algorithms could remarkably eliminate thick haze situations. However, they tended to over-enhance the result and generate artifacts due to an instinct for luminance deductions. Besides, natural environments were so complicated that conventional dehazing algorithms hardly overcame the compounded issues caused by natural events. For convenience, we illustrated low-visibility images captured in four unfavorable environments in Fig. 1. Dehazing algorithms usually worked well when applied to the hazy image captured during the day, such as an image illustrated in Fig. 1(a). However, dense haze and chromatic atmospheric light may degrade visibility, as shown in Figs. 1(b) and 1(c), respectively; generally, these issues made dehazing algorithms fail luminance and color restoration. Situations may become more complicated at night with haze and artificial light sources, as shown in Fig. 1(d).

Researchers proposed various methods to overcome the shortages of dehazing algorithms. However, these methods needed a run-through summary because the functions were sometimes similar and overlapped. For example, some research aimed at nighttime images [26], [27], [28], [29]. Nighttime images usually contained compounded issues, including non-uniform illumination resulting from artificial light sources, haze-like effects, and glow effects caused by the atmosphere and artificial light sources. Issues defined in the research were quite different; some focused on haze-like

effects while others did not. On the other hand, some research aimed at daytime images, such as dehazing-like algorithms proposed in [30] and [31]. There was also research focused on improving low-light environments without haze-like effects [35], [36], [37]; the primary techniques of these methods were quite different. Some research adopted feature fusion techniques [32], [33], [34]; some obeyed retinex theory [35], [36]. Meanwhile, some research focused on specific events; for example, capturing low-light images with a camera brought lots of noise in real-world situations owing to high ISO (sensitivity) settings. Some research focused on this situation, providing an optimized Bezier curve to the mapping scheme [38] or an additional denoise function while enhancing brightness [39]. Moreover, research in [40] concentrates on daytime and nighttime conditions. There was also research focused on estimating visibility [41].

Summarily, the problems associated with flawed images were similar but slightly different. Hence, the recovering algorithms' functions were also similar but aimed at different issues, making it challenging to have a distinct classification regarding their functions. Nevertheless, the goals of the above methods were the same: improving the visibility. In this study, we concentrated on limited phenomena: haze-like effects and natural illumination issues. Note that glow effects caused by artificial light sources were not the primary concern in this study; nevertheless, we used the image in Fig. 1(d) to test the performance associated with luminance enhancement.

As previously discussed, using dehazing algorithms to overcome complicated effects in natural environments resulted in two problems. We ascribe artifact issues to unstable performance and brightness degradations to the instinct of dehazing algorithms. Therefore, dehazing low-visibility images required additional luminance enhancements [42], [43], [44], [45]. Nevertheless, after some derivations, we conclude that dehazing algorithms can simultaneously solve haze and illumination issues in theory. We propose a novel framework to enhance low-visibility images and overcome low-illumination and dense haze conditions by repeatedly using a dehazing algorithm. The contributions of our research include the following:

- We propose clear derivations and analysis to demonstrate that dehazing algorithms can theoretically solve haze and illumination problems at the same time.
- Based on our theory, we proposed a novel enhancement framework.
- We also proposed a new dehazing algorithm with a novel transmission thresholding method because existing dehazing algorithms cannot stably produce quality-enhanced results under the proposed framework.

II. RELATED WORKS

A. DARK CHANNEL PRIOR

An atmospheric model describing the effects of the single and homogeneous scattering is formulated as follows:

$$I = Jt + A(1 - t), \quad (1)$$



FIGURE 2. (a) Low-visibility images caused by haze; (b) Dehazed image of (a) obtained using DCP [1]; (c) Negative image of (a); (d) Dehazed image of (c) obtained using our dehazing algorithm; (e) Positive image of (d); (f) Final enhanced image of (a) obtained using the proposed framework.

where I is a hazy image, t is the transmission, A is the global atmospheric light, and J is a dehazed image of the hazy image. The first and second terms on the right side in (1) are the direct attenuation and atmospheric terms, respectively. When both sides of (1) are divided by A , the result is as follows:

$$\hat{I} = \hat{J}t + (1 - t), \tag{2}$$

where the hat symbol denotes a variable divided by the global atmospheric light. After considering the minimal operator concerning the RGB color channels and a small patch in images, (2) can be rewritten as follows:

$$\begin{aligned} \min_{\Omega} \min_c \hat{I} &= \min_{\Omega} \min_c [\hat{J}t + (1 - t)] \\ &= \min_{\Omega} \min_c \hat{J}t + \min_{\Omega} (1 - t), \end{aligned} \tag{3}$$

where Ω denotes a small patch, and c represents RGB color channels. Dark channel prior (DCP) assumes that the lowest responses within Ω in a clear image are close to zero; therefore, we can obtain a preliminary estimate of the transmission roughly as follows:

$$\tilde{t} = 1 - \min_{\Omega} \min_c \hat{I}, \tag{4}$$

where \tilde{t} denoted the preliminary estimate. However, \tilde{t} needs further refinement to solve edge alignment problems caused by the patch-wise minima operator.

We follow the concept of DCP, except that we ignore the patch-wise minima operator. Accordingly, we rewrite (3)

as follows:

$$\min_c \hat{I} = \min_c \hat{J}t + (1 - t). \tag{5}$$

For convenience, we replace the minima operators in (5) with more straightforward symbols, as follows:

$$\hat{I}_{min} = \hat{J}_{min}t + (1 - t), \tag{6}$$

where \hat{I}_{min} and \hat{J}_{min} denote results obtained using the pixel-wise minima operator on corresponding images. Note that \hat{I}_{min} and \hat{J}_{min} are one kind of dark channel. Similar to (4), we obtain our preliminary estimate of the transmission as follows:

$$\tilde{t} = 1 - \hat{I}_{min}. \tag{7}$$

However, the preliminary estimate also needs refinements because of over-saturation problems. Refinements are usually implemented on \hat{I}_{min} ; accordingly, we denote a refined estimate of the transmission as follows:

$$t^r = 1 - \hat{I}_{min}^r, \tag{8}$$

where t^r and \hat{I}_{min}^r denote refined results of corresponding variables.

B. CONTRAST AND LUMINANCE IN HAZE REMOVAL

Note that when the minima operator in (6) is replaced with the maxima operator, the result is as follows:

$$\max_c \hat{I} = \max_c \hat{J}t + (1 - t). \tag{9}$$

Similarly, we rewrite (9) in the previous style and obtain the following:

$$\hat{I}_{max} = \hat{J}_{max}t + (1 - t). \tag{10}$$

Note that A and C are the HSV color space's value channels, indicating the brightness of corresponding images. After some derivations, (10) can be summarized as follows:

$$t = \frac{1 - \hat{I}_{max}}{1 - \hat{J}_{max}} = \frac{S_j}{S_j}, \tag{11}$$

where S_j and S_j respectively denote the negative images of \hat{I}_{max} and \hat{J}_{max} ; therefore, S_j and S_j represent the darkness of \hat{I} and \hat{J} . Besides the brightness relation, we obtain the contrast relation based on the gradient as follows:

$$\frac{S_j}{S_j} \propto \frac{\nabla \hat{I}_{max}}{\nabla \hat{J}_{max}}, \tag{12}$$

where ∇ is the gradient operator. The situation was first reported by Liu et al. [8], showing that when haze removal algorithms generate a contrasting dehazed image, the darkness of the dehazed image increases; otherwise, the dehazed image remains bright but unclear. Accordingly, Liu et al. proposed a theory that all dehazing algorithms based on the atmospheric model in (1) involve a trade-off between contrast rise and brightness degradation of the dehazed image.

III. THE PROPOSED METHOD

An example of Liu's theory is illustrated in Fig. 2. A low-visibility image and its dehazed result obtained using DCP are shown in Figs. 2(a) and 2(b), respectively. The dehazed result in Fig. 2(b) is more contrasting than the low-visibility image; however, the brightness of the dehazed image degrades. As a result, dehazing algorithms do not help overcome visibility issues caused by lowlight environments in most cases.

A. THE PROPOSED FRAMEWORK

The proposed framework involves two-time dehazing processes. According to (2), when dehazing the negative image of the hazy image, the process can be demonstrated as follows:

$$\hat{J}^n = 1 - \frac{1 - \hat{I}^n}{t^n}, \quad (13)$$

where \hat{I}^n is the negative image of \hat{I} , and t^n is the corresponding transmission. To simplify (13), we use a fixed global atmospheric light A^n of which all RGB values are defined as one. Since RGB values of A^n are one, the above equation is equivalent to the following:

$$J^n = 1 - \frac{1 - I^n}{t^n}, \quad (14)$$

where I^n is the negative image of I . We illustrated corresponding experimental results in Fig. 2. A negative image and a corresponding dehazed result obtained using our dehazing algorithm are shown in Figs. 2(c) and 2(d), respectively. The experimental results comply with Liu's theory, so the image's contrast in Fig. 2(d) rises while brightness degrades. Note that (14) can be rewritten when replacing the negative images with corresponding positive images and is equivalent to the following:

$$J^* = \frac{I}{t^n}, \quad (15)$$

where J^* is the positive image of J^n and also a preliminarily-enhanced result of I . The fact that t^n is less than one guarantees that J^* is more contrasting and brighter than I . Therefore, we conclude that inputting a negative image to dehazing algorithms helps raise contrast and brightness. An example shown in Fig. 2(e) clearly illustrates this phenomenon. The process of dehazing a negative image and retrieving the positive image of the dehazed result using (15) can be considered a particular case in Liu's theory. Since dehazing algorithms lower the brightness of the input to enhance the contrast, they should raise the brightness to improve contrast in an inverted case using (15). Therefore, the positive image in Fig. 2(e) is brighter and more contrasting than the original image in Fig. 2(a).

On the other hand, the dehazed result of J^* can be obtained as follows:

$$J^{**} = A^* - \frac{A^* - J^*}{t^*}, \quad (16)$$

where J^{**} denote the dehazed image obtained from J^* . Fig. 2(f) demonstrates a final result obtained using the proposed framework. The final result is brighter and more contrasting when compared with the low-visibility image in Fig. 2(a); meanwhile, the final result is superior in visibility compared with the dehazed and preliminarily-enhanced results in Figs. 2(b) and 2(e), respectively. However, unlike dehazing the negative image in (14), the global atmospheric light should be estimated accurately to overcome color deviations caused by colorful scattered light.

B. OUR DEHAZING ALGORITHM

Previous discussions indicate that the proposed framework improves the visibility degraded by haze and unideal illumination. After some experiments, we found that the stable performance of dehazing algorithms is the crucial bottleneck of the proposed framework. Generally, deep-learning-based dehazing algorithms are more stable than conventional dehazing algorithms in performance, generating dehazed images of consistent quality. However, deep-learning-based dehazing algorithms sometimes disobey Liu's theory because they use the end-to-end architecture not derived from the atmospheric model in (1); therefore, they do not comply with our theory and are incompatible with the proposed framework. On the contrary, conventional algorithms lack stability, usually resulting in over-enhancement when included in the proposed framework. As a result, a configurable dehazing algorithm able to control levels of dehazing intensity is necessary.

The transmission is commonly assumed to be smooth in a small region because the region is related to the object's surface, not the texture [1], [2], [3], [4]. According to (2), we use the following equation to describe the gradient in a small region:

$$\nabla \hat{I} = \nabla \hat{J} t \quad \forall P, \quad (17)$$

where P denotes pixels in a small region. The equation shows that gradient degradations are highly related to the transmission at P ; therefore, we can estimate transmission levels from the gradient strength based on the high-frequency component of the hazy image. We denote a high-frequency component of I as L^h and conclude a relation as follows:

$$t \propto L^h. \quad (18)$$

The relation indicates that the transmission should positively correlate to gradients within a small region. We compute the pixel-wise geometric mean among RGB channels of I , and the result I_m can be obtained as follows:

$$I_{m,x} = \left(\prod_{y \in c} I_{x,y} \right)^{1/3} \quad \forall x \in I, \quad (19)$$

where x denotes a pixel, c denotes RGB color channels, and y represents a color channel; note that we calculate I_m from the hazy image, not the normalized one. Low-frequency components of I_m can be obtained using smoothing algorithms.

Algorithm 1 Estimate High-frequency Component

input: image I
 parameters: $S_r = 3, \eta = 0.005$
 output: high-frequency component L^h

Calculate L_m according to (19) and (20)

$$T_1^0 \leftarrow L_m$$

$$T_1^0 \leftarrow L_m$$

// Iterative Smoothing Step
 for $i = 1$ to S_r
 $T_2^i \leftarrow \varphi_i(T_1^{i-1}, T_2^{i-1}, 2^i)$
 $T_1^i \leftarrow \varphi_i(T_2^i, T_1^{i-1}, 2^i)$
 end
 $L_l \leftarrow L_{m1}^{S_r}$

Calculate L_h according to (23)

We conduct the following processes in the natural logarithm domain to avoid negative values. Accordingly, L_m is defined as follows:

$$L_m = \ln(I_m). \tag{20}$$

Similarly, \hat{I}_{min} is transformed into the natural logarithm domain as follows:

$$L_{dc} = \ln(\hat{I}_{min}), \tag{21}$$

where L_{dc} is an initial estimate of the final dark channel. We import Shen’s method [46] as a smoothing algorithm. Shen et al. reported that their algorithm could identify joint edges simultaneously occurring in two inputs and preserve the joint edges. Shen’s method relies on ridge regression, which fits one image to another, and the core technology is the guided image filter (GIF) [47]. The process of GIF is defined as follows:

$$\arg \min_{a_x, b_x} \sum_{\Omega} (a_x M_{\Omega_x} + b_x - N_{\Omega_x})^2 + \eta |a_x|^2, \tag{22}$$

where Ω_x denotes a sliding patch in images M and N , x represents the center of Ω_x , a_x and b_x are two parameters, and η controls the shrinkage term. The output of GIF has similar gradients as M and intensity levels as N . We denote GIF as $\varphi(M, N, r)$, where r denotes the radius of Ω_x and η is set to a default value of 0.005. Shen’s method uses GIF and iteratively switches the roles of the two inputs to obtain a smooth result. The smoothing result, denoted as L^l , is a low-frequency component of L_m . After that, a high-frequency component representing gradient changes on the object’s surfaces is obtained as follows:

$$L_h = L_m - L_l. \tag{23}$$

Algorithm 1 demonstrates the detail of estimating L_h . Although the two inputs of $\varphi()$ are the same in Algorithm 1, they both get smoothing because of the shrinkage term.

Algorithm 2 Refinement

input: initial estimate L_{dc}
 preliminary estimate P_{dc}
 parameters: $S_R = 6, \eta = 0.005$
 output: refined estimate \tilde{L}_{dc}

$$T_1^0 \leftarrow P_{dc}$$

$$T_2^0 \leftarrow L_{dc}$$

// Iterative Refining Step
 for $i = 1$ to S_R
 $T_2^i \leftarrow \varphi_i(T_1^{i-1}, T_2^{i-1}, 2^i)$
 $T_1^i \leftarrow \varphi_i(T_2^i, T_1^{i-1}, 2^i)$
 end
 $\tilde{L}_{dc} \leftarrow T_1^i$

We aim to estimate the object’s surfaces by eliminating gradient changes at the chosen scale. Accordingly, the iterative smoothing step starts from small patches to guarantee the input’s smoothness at the fine scale; this helps the accuracy of the input’s smoothness at the coarse scale. Since gradient changes on the object surface correlate to the transmission according to (18), we obtain a preliminary estimate of the final result according to the following:

$$P_{dc} = L_{dc} - \alpha |L_h|, \tag{24}$$

where P_{dc} denotes the preliminary estimate, and α controls dehazing levels as a scale factor of L^h ; the detail is based on (8) and can be demonstrated as follows:

$$\tilde{t} \propto 1 - e^{P_{dc}} = 1 - \hat{I}_{min} e^{-\alpha |L_h|}. \tag{25}$$

The equation demonstrates that our dehazing algorithm produces transmission estimates positively related to $|L_h|$; this complies with (18). Moreover, α controls the level of transmission estimate; this is very useful in preventing over-enhancements. A refined estimate can be obtained using Shen’s method, as demonstrated in Algorithm 2; we denote the refined estimate as \tilde{L}_{dc} . Afterward, our transmission estimate can be obtained as follows:

$$\tilde{t} = 1 - e^{\tilde{L}_{dc}}, \tag{26}$$

Eventually, we compute a dehazed image according to the atmospheric model in (1).

C. ADAPTIVE THRESHOLD TO TRANSMISSION

As previously discussed, over-enhancements are a common issue of dehazing algorithms, especially for those who cannot adapt to the complexity of natural scenes. Accordingly, the thresholding to the transmission is necessary [1], [2], [3], [4], and a fixed threshold of 0.9 is commonly used to prevent over-saturation in the sky or low-light regions. However, a fixed threshold is not adaptive enough to complicated situations. Fortunately, sky regions are highly correlated to

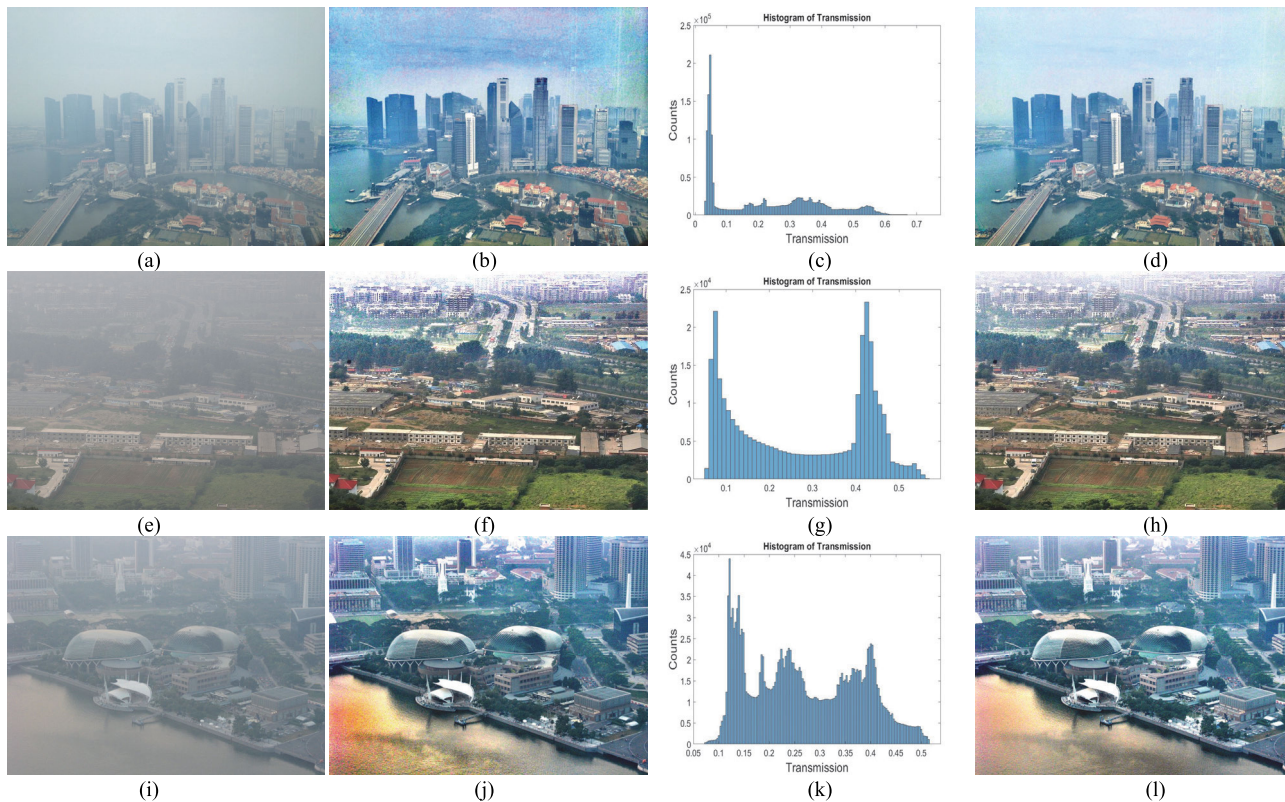


FIGURE 3. (a) (e)(i) Low visibility images containing vast sky regions, narrow sky regions, and no sky region, respectively; (b)(f)(j) Enhanced results with a fixed threshold of 0.9 obtained from (a), (e), and (i), respectively; (c)(g)(k) Histograms of transmission of (a), (e), and (i), respectively; (d)(h)(l) Enhanced results using thresholding obtained from (a), (e), and (i), respectively.

the compositions of images. Vanishing points are the most significant feature able to recognize scene structures. Images containing vanishing points in the center have vast sky regions, such as a low-visibility image illustrated in Fig. 3(a). We enhance the low-visibility image using the proposed framework based on our dehazing algorithm; as a result, we draw the distribution of our transmission estimate in a histogram in Fig. 3(c). The histogram skews to the right, meaning that the transmission estimate gathers in an interval from 0 to 0.1. The proposed framework over-enhances sky regions with a fixed threshold of 0.9, as illustrated in Fig. 3(d). Over-enhancements in sky regions are evident, needing further remedies to reduce noises, artifacts, and the loss of brightness. In another case, sky regions in a low-visibility image illustrated in Fig. 3(e) are narrow and tend to over-expose after enhancing using the proposed framework with a fixed threshold of 0.9, as demonstrated in Fig. 3(f). The histogram of our transmission estimate based on the low-visibility image is illustrated in Fig. 3(g) and is a bimodal distribution. Transmission estimates' distributions of images in Figs. 3(b) and 3(f) are highly correlated to the area of sky regions and depend on vanishing points. A low-visibility image illustrated in Fig. 3(i) oppositely has no vanishing points and sky regions. In an enhanced result obtained using the proposed framework with a fixed threshold of 0.9, degradations from over-enhancements barely happen, as demonstrated in Fig. 3(j). The enhancement case works

fine because of the smoother transmission estimate's distribution, as shown in Fig. 3(k).

In conclusion, different issues among the above-mentioned enhancing cases result from the distribution of transmission estimates. Low-visibility images containing vast sky regions involve transmission estimates of long-tail distributions skewing to the right. On the contrary, narrow sky regions result in transmission estimates of bimodal distributions. Since over-enhancements result from low transmission estimates, the distribution of transmission estimates determines the optimal thresholding. The k-means clustering algorithm is thereby applied to the histogram of \hat{I}_{min} to cluster transmission estimates into several categories as follows:

$$\arg \min_{x_i} \sum_{n_i \in N} \sum_{x_i \in n_i} (x_i - \mu_i)^2 \quad \forall x_i \in \hat{I}_{min}, \quad (27)$$

where n_i denotes a category in a set N ; x_i indicates pixels belonging to n_i ; μ_i is the mean of n_i ; i represents the number of elements in N and is set to a default value of 3. Afterward, the optimal threshold can be obtained as follows:

$$t_{th} = \frac{1}{2}(\mu_1 - \mu_2), \quad (28)$$

where t_{th} denotes the transmission threshold, μ_1 and μ_2 respectively represent the first and secondary minima among μ_i . Enhanced results based on our thresholding method are illustrated in Figs. 3(d), 3(h), and 3(l). Our thresholding method suppresses over-enhancements in Fig. 3(c) and

Algorithm 3 The Proposed Framework

input: love-visibility image I
 parameters: $s = 30, v = 90, a^n = 12, a^p = 10$

output: enhanced image J^{**}
 Calculate L_h according to Algorithm 1
 Obtained the negative image I^n from I

// Step 1 Compute the Preliminarily-enhanced Result J^*
 // Dehazing Process to the Negative Image I^n
 Define the global atmospheric light A^n as (1,1,1)
 Obtain I_{min}^n from I
 Calculate P_{dc}^n according to (24) using a^n and L_h
 Calculate \tilde{I}_{dc}^n according to Algorithm 2
 Calculate \tilde{t}^n according to (26)
 Calculate J^* according to (15) and \tilde{t}^n

// Step 2 Compute the fully-enhanced Result J^{**}
 // Dehazing Process to J^*
 Estimate the global atmospheric light A^* from J^*
 Obtain \hat{J}_{min}^* from J^* and A^*
 Calculate P_{dc}^* according to (24) using a^p and L_h
 Calculate \tilde{I}_{dc}^* according to Algorithm 2
 Calculate \tilde{t}^* according to (26)
 Compute threshold according to (27) and (28)
 Thresholding \tilde{t}^*
 Calculate J^{**} according to (16) and \tilde{t}^*

over-exposures in Fig. 3(g); meanwhile, in a well-enhanced case, our thresholding method keeps image quality in 3(l). With the help of our thresholding method, the proposed framework enhances the visibility of images by all means. The proposed framework prevents noise and artifact amplifications and improves visibility without harming image quality; this is the primary difference between conventional dehazing algorithms and ours. Although some hazy regions are still hazy in the corners or borders of the image, visibility has risen substantially due to brightness improvements.

D. ESTIMATE GLOBAL ATMOSPHERIC LIGHT

A global atmospheric light’s estimate is conventionally computed from the brightest pixels; however, many low-visibility images have over-exposure issues, so the estimated global atmospheric light may hugely deviate from the truth. To prevent deviations caused by over-exposures, we estimate the color of the global atmospheric light from pastel-color pixels because these pixels are most likely to have the same color as the global atmospheric light. First, we assess the pastel color according to saturation defined in HSV color space as follows:

$$S = \frac{I_{max} - I_{min}}{I_{max} + I_{min}}, \tag{29}$$

where S is the HSV saturation. The color of the global atmospheric light is then calculated as follows:

$$C_A = \frac{1}{N_i} \sum_i I_i \forall S_i < P_s, \tag{30}$$

where C_A denotes the estimated color of the global atmospheric light; i and N_i respectively denote a pixel set and the number of the pixel set; P_s denotes the s -th percentile of the HSV saturation channel. After that, we transform C_A into the HSV color space, and the result is denoted as A_{hsv} to await a new brightness assignment. We choose pixels most likely to lie in the deepest regions by thresholding I_{min} ; afterward, the average luminance of the selected pixels should represent the brightness of the global atmospheric light, as follows:

$$V_A = \frac{1}{N_i} \sum_i I_{max,i} \quad \forall I_{min,i} > P_v \tag{31}$$

where V_A denotes the value channel’s estimate of the global atmospheric light; i and N_i respectively denote a pixel set and the number of the pixel set; P_l denotes the v -th percentile of I_{min} . Eventually, we replace the value channel of A_{hsv} with V_A and transform A_{hsv} back to the RGB color space again as the final atmospheric light estimate. Note that s and v are set to default values of 30 and 90, respectively.

E. ALGORITHM

Algorithm 3 demonstrates the overall algorithm of the proposed framework, which includes two steps. The first step involves brightness and contrast enhancement; we calculate the negative image of a low-visibility image and estimate the transmission of the negative image based on (19)-(26). After that, we calculate a preliminarily-enhanced result of the low visibility image according to (15); note that the preliminarily-enhanced result is a positive image. The second step is a typical dehazing process, which reduces brightness and raises contrast; we estimate the transmission of the preliminarily enhanced result and use the transmission estimate to compute the final enhanced result. Eventually, we obtain a bright and contrasting enhanced result.

IV. EXPERIMENTAL RESULTS

A. GOALS AND SETUP OF EXPERIMENTS

The proposed framework involves dehazing processes twice, as demonstrated in Algorithm 3; therefore, if a dehazing algorithm we choose tends to over-enhance the inputs, outputs worsen twice. Thus, the performance associated with the structure similarity and color deviations is essential for the proposed framework and highly correlates to enhancement quality; accordingly, we evaluate the performance of our approaches in several benchmarks in this section. However, the proposed framework is developed based on the intrinsic property of the atmospheric model in (1), so our experiments only focus on evaluations of corresponding dehazing algorithms, including the dark channel prior (DCP) [1], boundary constraint and contextual regularization (BCCR) [2], color

TABLE 1. Quality evaluation of dehazing processes.

Benchmark	Dataset	DCP [1]	BCCR [2]	CAP [3]	NLD [4]	DN [5]	AOD [7]	CIH [8]	MSCN [6]	GFN [9]	PDN [10]	CEE [12]	Our dehaze
SSIM	SOTS	0.8418	0.7862	0.8796	0.7752	0.8525	0.8673	0.8613	0.8340	0.8673	0.8647	0.7519	0.8971
-Luminance	SOTS	0.9256	0.8895	0.9148	0.8846	0.8778	0.9090	0.9068	0.8780	0.9140	0.9067	0.8221	0.9267
-Contrast	SOTS	0.9389	0.9144	0.9756	0.9324	0.9818	0.9715	0.9699	0.9639	0.9720	0.9717	0.9187	0.9760
-Structure	SOTS	0.9708	0.9618	0.9842	0.9287	0.9865	0.9710	0.9720	0.9814	0.9618	0.9786	0.9861	0.9895
F&T	SOTS	0.8543	0.8590	0.8628	0.8707	0.8728	0.8638	0.8453	0.8748	0.8559	0.8475	0.8274	0.8863
DehazeFR	SOTS	0.9574	0.9704	0.9560	0.9767	0.9635	0.9591	0.9715	0.9455	0.9859	0.9751	0.9192	0.9861
MSE	SOTS	0.0181	0.0280	0.0109	0.0217	0.0086	0.0152	0.0181	0.0185	0.0094	0.0128	0.0273	0.0110
PSNR	SOTS	18.761	16.304	20.608	17.680	22.369	19.156	18.642	18.369	21.927	18.975	16.406	22.118
CieDE2000	SOTS	8.9463	11.361	7.0421	10.807	6.0653	7.9620	8.7300	9.1860	6.1328	7.7502	12.507	6.0380
SSIM	HRD	0.6055	0.6796	0.6385	0.6393	0.6027	0.6005	0.6680	0.6470	0.5168	0.6360	0.4888	0.7211
-Luminance	HRD	0.8750	0.9215	0.9172	0.9013	0.8734	0.8961	0.9081	0.9168	0.7448	0.9010	0.8062	0.9169
-Contrast	HRD	0.7353	0.7780	0.7265	0.7818	0.7459	0.7142	0.7922	0.7234	0.7589	0.7369	0.6734	0.8012
-Structure	HRD	0.9628	0.9495	0.9487	0.8739	0.9205	0.9463	0.9232	0.9647	0.9222	0.9312	0.9312	0.9710
F&T	HRD	0.7969	0.7862	0.7898	0.8165	0.7956	0.7938	0.8105	0.7961	0.8101	0.8115	0.8057	0.8224
DehazeFR	HRD	0.8482	0.8950	0.8128	0.9045	0.8305	0.8075	0.9105	0.8126	0.8913	0.7937	0.8577	0.9160
MSE	HRD	0.0388	0.0358	0.0395	0.0443	0.0375	0.0339	0.0294	0.0386	0.0513	0.0403	0.0390	0.0312
PSNR	HRD	14.661	15.147	15.506	14.576	15.344	15.473	16.113	15.700	13.813	14.625	15.832	16.203
CieDE2000	HRD	14.967	13.853	14.229	15.046	14.485	14.395	12.058	13.524	16.277	14.494	16.634	11.900

Bold: the best result among the tested algorithms

attenuation prior (CAP) [3], non-local image dehazing (NLD) [4], DehazeNet (DN) [5], AOD-net (AOD) [7], and contrast in haze removal algorithm (CIH) [8]. Moreover, we also test four deep-learning-based dehazing algorithms, including the multi-scale convolutional neural networks (MSCN) [6], gated fusion network (GFN) [9], proximal Dehaze-Net (PDN) [10] and contrast enhancement and exposure fusion algorithm (CEE) [12]. We download codes of the dehazing algorithms mentioned above from the authors' websites and use several benchmarks to evaluate the performance of each dehazing algorithm. Full-reference benchmarks include the mean square error (MSE), the peak signal-to-noise ratio (PSNR), the structural similarity index (SSIM) [14], and the CIEDE2000 [15]. MSE is the L2-errors between the ground truth and dehazed image, and PSNR indicates the ratio between the maximal response and MSE. Note that PSNR measures how the strength of the signal contributes to the noise so that it can assess the ability of the noise control. However, according to the definition, MSE and PSNR are not sensitive to artifacts, structural similarity, and color deviation [49]; therefore, we use SSIM and CIEDE2000 to evaluate the structural similarity and color deviations, respectively. Besides, F&T is a feature-based assessment composed of FSITM [50] and TMQI [51] and assesses features in the frequency domain for comparison with benchmarks functioning in the spatial domain. Moreover, we use the regular DehazeFR [52] to evaluate the performance regarding structure recovery, color renditions, and suppression of over-enhancement. Non-reference benchmarks include the perception-based image quality evaluation (PIQE) [17], non-reference image quality assessment (NRIQA) [18], and blind image quality evaluation (BIQE) [19]; these benchmarks evaluate image quality in terms of contrast, brightness, and

image naturalness. All benchmarks are calculated using MATLAB 2021a under Windows 10 environment. Eventually, we conduct the evaluations on two datasets, including the synthetic objective testing set (SOTS) [21] and the HazeRD dataset (HRD) [53]. Furthermore, we also collect low-visibility images from previous research and the internet. Our dataset comprises 20 low-visibility images and is used to evaluate the proposed framework based on different dehazing algorithms. Unless specifically mentioned, the proposed framework uses default parameters, as demonstrated in Algorithms 1-3.

B. EVALUATION OF DEHAZING PROCESS

We experiment to evaluate the performance of our dehazing method, and we give α as a value of 9. In the experiment, our and several conventional dehazing algorithms are applied to hazy images in SOTS and HRD. Corresponding dehazed images are evaluated using full-reference benchmarks, and the benchmark results are demonstrated in Table 1. Our dehazing algorithm is superior in quality restoration regarding structural similarity and color because of outstanding SSIM and CIEDE2000 results respectively. The benchmark results indicate that our dehazing algorithm results in accurate color and fewer artifacts; this is very important to prevent color deviations and structural impairments. On the other hand, our dehazing method is relatively weak in MSE, while DN shows noticeable performance. However, the PSNR indicates that our dehazing algorithm has a comparable ability to DN concerning noise control. Besides, although results obtained using DN show noticeable improvements concerning MSE and PSNR, conventional dehazing algorithms strongly tend to degrade brightness. We evaluate several dehazing algorithms using our dataset. Tested



FIGURE 4. (a) Comparisons associated with contrast and brightness between 20 low-visibility images (Raw) and corresponding enhanced results of conventional dehazing algorithms. The size of circles indicates the performance associated with the geometric mean of PIQE, NRIQA, and BIQE; (b)(c)(d)(e) Low-visibility images; (f) Comparisons associated with the performance of DCP; (g)(h)(i)(j) Enhanced results of DCP; (k) Comparisons associated with the performance of MSCN; (l)(m)(n)(o) Enhanced results of MSCN; (p) Comparisons associated with the proposed framework; (q)(r)(s)(t) Enhanced results based on the proposed framework.

TABLE 2. Quality evaluation of enhancement processes based on dehazing algorithms.

Benchmark	Raw	DCP [1]	BCCR [2]	CAP [3]	NLD [4]	DN [5]	AOD [7]	CIH [8]	MSCN [6]	Proposed
Cont.Y	0.0302	0.0417	0.0441	0.0338	0.0578	0.0352	0.0363	0.0564	0.0381	0.0709
Cont.Cb	0.0113	0.0144	0.0141	0.0120	0.0153	0.0120	0.0123	0.0122	0.0125	0.0169
Cont.Cr	0.0110	0.0137	0.0132	0.0115	0.0143	0.0115	0.0118	0.0118	0.0118	0.0158
Brightness	0.5029	0.2966	0.3047	0.3649	0.3366	0.3438	0.3148	0.3875	0.3857	0.5374
PIQE	32.7584	40.7694	38.5649	42.4510	36.5999	41.7594	43.8634	37.7131	41.0104	31.2413
NRIQA	28.1474	30.7320	28.4609	32.5269	31.5254	32.4432	30.5224	27.8726	31.5056	26.6569
BIQE	2.9171	2.9232	2.9844	3.0936	2.9395	3.0059	3.1258	2.8299	3.0002	2.5807
NR_geoM	13.6390	15.2923	14.5588	16.0926	14.7891	15.8321	15.9771	14.2091	15.5825	12.6699

Bold: the best result among the tested algorithms
 NR_geoM: the geometric mean of non-reference benchmarks concerning the tested algorithms

algorithms include DCP, BCCR, CAP, NLD, DN, AOD, CIH, MSCN, and the proposed framework based on our dehazing algorithm. This experiment evaluates the corresponding enhanced results' contrast, brightness, and image quality. Accordingly, we assess contrast levels by the mean of the standard deviation from every 15*15 patch in YCbCr channels and brightness levels by the average of the Y channel;

meanwhile, we evaluate image quality by PIQE, NRIQA, and BIQE; these represent the quality in contrast, brightness, and image naturalness. Table 2 demonstrates the results of the experiment.

Based on the experimental results, Fig. 4 illustrates crucial differences between conventional dehazing algorithms and the proposed framework. The first row in Fig. 4 shows four

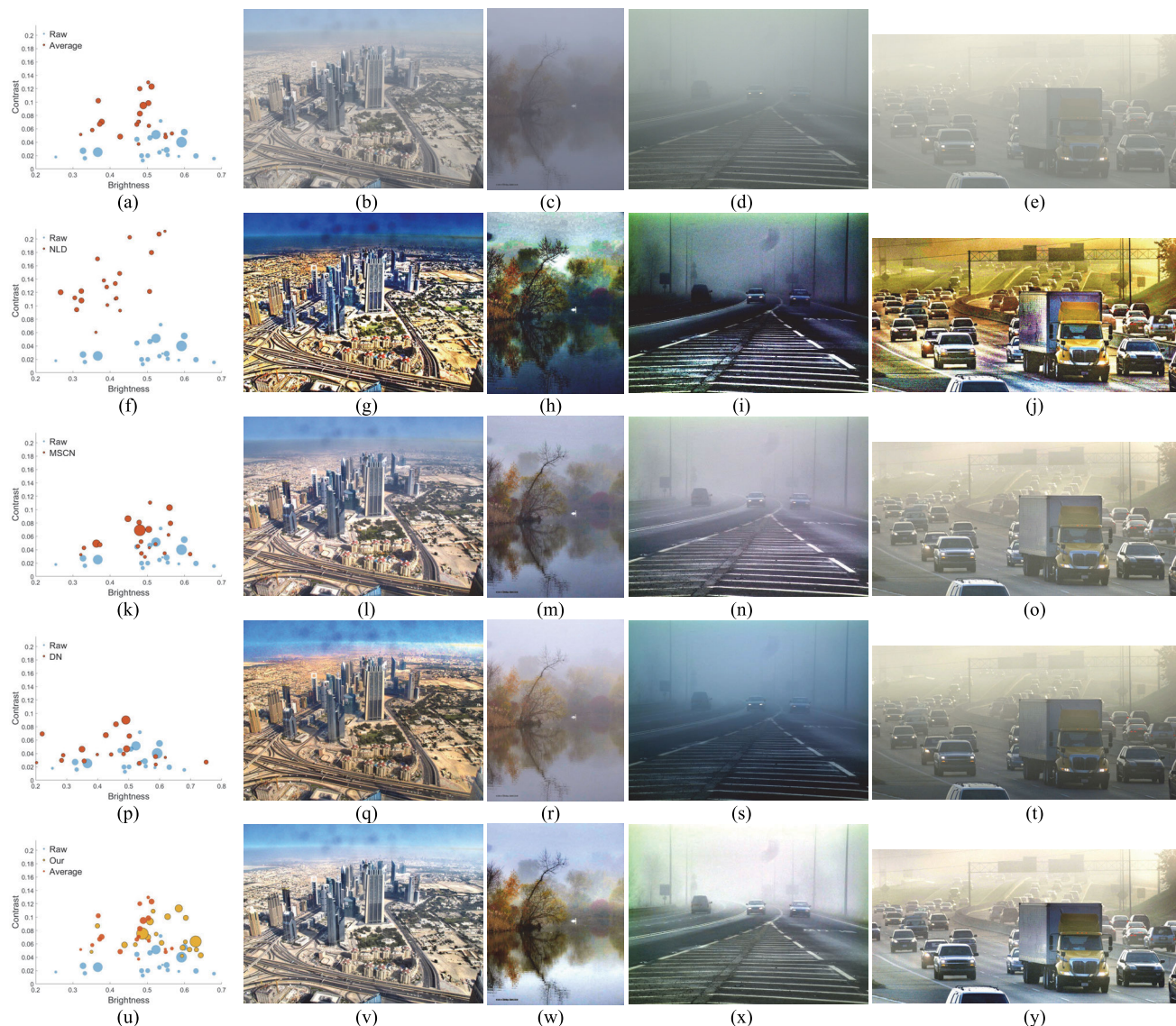


FIGURE 5. (a) Comparisons associated with contrast and brightness between 20 low-visibility images (Raw) and corresponding enhanced results obtained collaboratively using the proposed framework and dehazing algorithms. The size of circles indicates the performance associated with the geometric mean of PIQE, NRIQA, and BIQE; (b)(c)(d)(e) Low-visibility images; (f) Comparisons associated with enhanced results of NLD; (g)(h)(i)(j) Enhanced results of NLD; (k) Comparisons associated with enhanced results of MSCN; (l)(m)(n)(o) Enhanced results of MSCN; (p) Comparisons associated with enhanced results of DN; (q)(r)(s)(t) Enhanced results of; (u) Comparisons associated with the proposed framework; (v)(w)(x)(y) Enhanced results of the proposed framework.

low-visibility images in our dataset with low illumination or exposures, and the following rows show enhanced results obtained using several methods, including DCP, MSCN, and the proposed framework based on our dehazing algorithm. The chart in Fig. 4(a) compares the contrast and brightness evaluations between raw images (low-visibility images) and corresponding enhanced results based on all dehazing algorithms. We use blue to represent assessments for raw images and red for enhanced results obtained using dehazing algorithms. The scattered points of the same color indicate evaluations of images in our dataset by a specific method (or raw images), and the size of the scattered points represents the geometric mean among PIQE, NRIQA, and BIQE.

Accordingly, enhanced results obtained using the tested dehazing algorithms are significantly darker than the raw images while their contrast rises. As a result, the image quality of the enhanced results degrades when compared with that of raw images. The same phenomenon occurs in enhanced results obtained using DCP and MSCN, as illustrated in Figs. 4(f) and 4(k). On the contrary, enhanced results based on the proposed framework are brighter and more contrasting than others. Fig. 4(p) illustrates the assessment associated with the proposed framework. Our non-reference benchmark results demonstrated in Table 2 prove that contrast and brightness improvements favor image quality significantly; this can be observed from our enhanced results shown

TABLE 3. QUALITY evaluation of compounded enhancement processes I.

Benchmark	Raw	DCP + Ours	BCCR + Ours	CAP + Ours	NLD + Ours	DN + Ours	AOD + Ours	CIH + Ours	MSCN + Ours	Proposed
Cont.Y	0.0302	0.0641	0.1031	0.0430	0.1338	0.0471	0.0531	0.1020	0.0577	0.0709
Cont.Cb	0.0113	0.0231	0.0260	0.0145	0.0319	0.0148	0.0156	0.0158	0.0160	0.0169
Cont.Cr	0.0110	0.0213	0.0236	0.0138	0.0299	0.0140	0.0147	0.0149	0.0151	0.0158
Brightness	0.5029	0.4898	0.4499	0.4608	0.4035	0.4484	0.5425	0.4260	0.4804	0.5374
PIQE	32.7584	34.0690	32.6174	37.7257	39.4176	38.1520	43.7664	37.2758	38.3049	31.2413
NRIQA	28.1474	29.8033	28.7576	32.5727	28.3875	31.3209	34.3954	28.4524	30.1425	26.6569
BIQE	2.9171	2.9987	2.4863	2.9324	3.7487	2.8477	3.4839	2.9708	2.9324	2.5807
NR.geoM	13.6390	14.0296	14.5414	15.2194	15.7711	14.8782	17.1553	14.3625	14.7947	12.6699

Bold: the best result among the tested algorithms
 NR.geoM: the geometric mean of non-reference benchmark concerning the tested algorithms

TABLE 4. Quality evaluation of compounded enhancement processes II.

Average Benchmark	Cont.Y	Cont.Cb	Cont.Cr	Brightness	PIQE	NRIQA	BIQE	NR.geoM
Dehaze + BIMEF	0.0532	0.0142	0.0134	0.4745	41.1638	33.2748	3.1382	16.2593
Dehaze + JED	0.0550	0.0166	0.0157	0.5393	43.3904	27.4654	3.4530	16.0247
Dehaze + FBE	0.0607	0.0163	0.0152	0.4945	40.4989	33.6328	3.3807	16.6369
Dehaze + LIME	0.0691	0.0182	0.0170	0.5511	38.9710	31.8506	3.4404	16.2240
Proposed	0.0709	0.0169	0.0158	0.5374	31.2413	26.6569	2.5807	12.6699

Bold: the best result among the tested algorithms
 NR.geoM: the geometric mean of non-reference benchmarks concerning the tested algorithms

in Figs. 4(q)-4(t). In conclusion, our dehazing algorithms outperform conventional algorithms in most restoration assessments and all evaluations associated with image quality. Conventional dehazing algorithms result in brightness degradation and sometimes harm image quality; however, the proposed framework based on our dehazing algorithm overcomes this issue, producing bright, contrast, natural, and quality-enhanced results; this makes conventional dehazing algorithms hardly comparable to the proposed framework.

C. EVALUATION OF ENHANCEMENT FRAMEWORK

We also test each conventional dehazing algorithm's compatibility with the proposed framework. In this experiment, we implement the dehazing process demonstrated in Algorithm 3 with conventional dehazing algorithms, and Table 3 shows corresponding experimental results. Contrast improvements associated with BCCR, NLD, and CIH are superior to our dehazing algorithm; nevertheless, the contrast improvements do not positively affect image quality according to their PIQE, NRIQA, and BIQE results. A similar situation happens in brightness evaluations; AOD produces enhanced results of higher brightness but unsatisfactory image quality. We illustrated some enhanced results in Fig. 5 to show the phenomenon. We present four low-visibility images in the first row of Fig. 5; similar to Fig. 4(a), the chart in Fig. 5(a) compares the contrast and brightness evaluations

between raw images (low-visibility images) and enhanced results obtained by all dehazing algorithms based on the proposed framework. The brightness of enhanced results rises with the help of the proposed framework; however, the size of the scattered points indicates that the average image quality degrades. For example, NLD produces enhanced results of high contrast; however, these results are usually over-enhanced. Figs. 5(f)-5(j) show this phenomenon. Over-enhancement is the decisive reason that NLD, BCCR, and CIH fail in image quality assessments. Also, note that color deviations in enhanced results cause errors in global atmospheric light estimates, and the errors are amplified two times according to Algorithm 3. Nevertheless, our thresholding method overcomes these issues, helping our dehazing algorithm to prevent over-enhancements.

D. MORE COMPARISONS

At last, we use several low-light enhancement algorithms to collaborate with conventional dehazing algorithms, attempting to raise the brightness of corresponding enhanced results. The low-light enhancement algorithms include bio-inspired multi-exposure fusion framework (BIMEF) [33], joint enhancement and denoising method (JED) [16], fusion-based enhancing method (FBE) [32], and low-light image enhancement via illumination map estimation (LIME) [35]. Unfortunately, experimental results are unsatisfactory

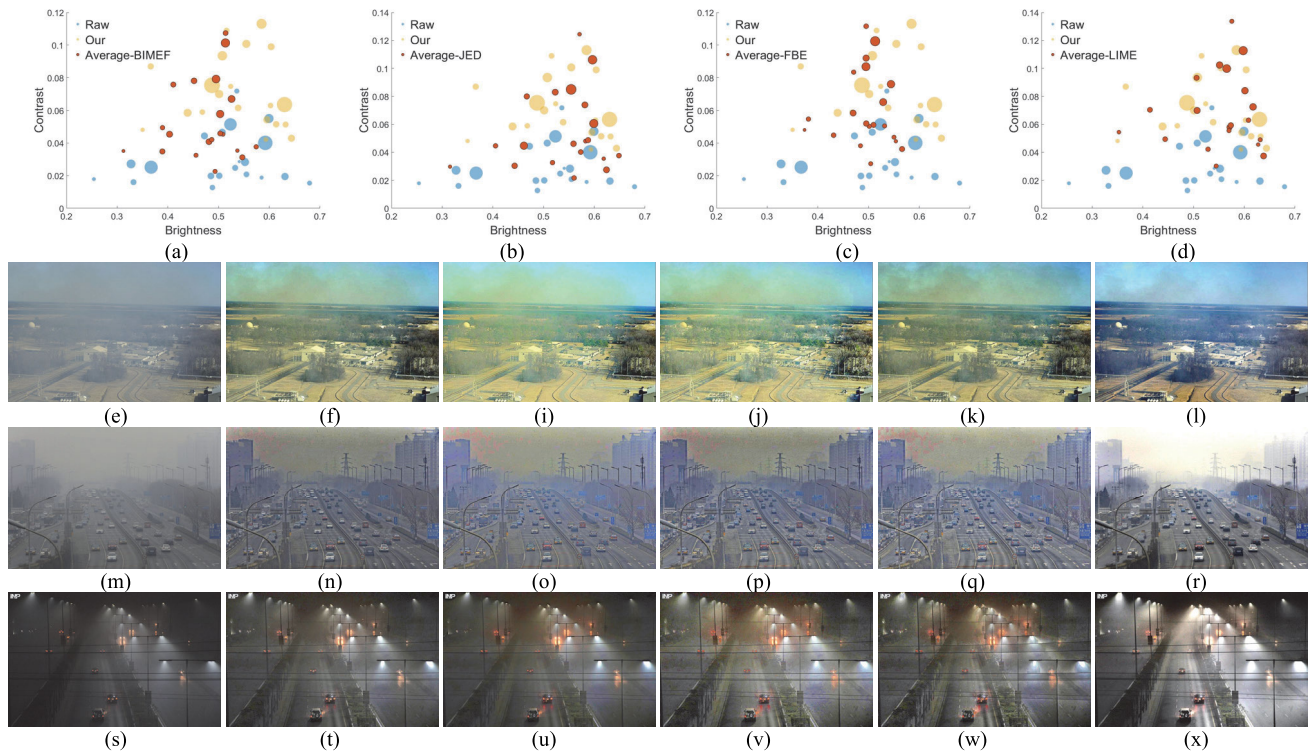


FIGURE 6. (a) (b)(c)(d) Comparisons associated with contrast and brightness between 20 low-visibility images (Raw) and corresponding enhanced results obtained collaboratively using dehazing algorithms and low-light enhancement methods. The size of circles indicates the performance associated with the geometric mean of PIQE, NRIQA, and BIQE; (e)(m)(s) Low-visibility images; (f)(i)(j)(k) Results of NLD enhanced using BIMEF, JED, FBE, and LIME, respectively; (n)(o)(p)(q) Results of BCCR enhanced using BIMEF, JED, FBE, and LIME, respectively; (t)(u)(v)(w) Results of AOD enhanced using BIMEF, JED, FBE, and LIME, respectively; (l)(r)(x) Enhanced results of the proposed framework. Note that we obtained (x) using $\alpha^n=3$ to raise the brightness.

because of the noise level and artifacts. Low-visibility images are taken under unideal conditions and usually contain lots of noise owing to the camera's high ISO setting. Meanwhile, JPEG compression also results in unnoticeable but complicated artifacts, so over-enhancements worsen the artifacts, especially those in dark or sky regions. As a result, image quality degrades. Table 4 demonstrates the phenomenon, and Fig. 6 illustrates the corresponding results. The red points in Figs. 6(a)-6(d) represent each enhanced result obtained collaboratively using conventional dehazing and low-light enhancement algorithms. The brightness and contrast of these enhanced results are comparable to ours; however, the size of these points indicates that image quality degrades, as non-reference benchmark results demonstrated in Table 4. Noise and artifacts result in the phenomenon. The second, third, and fourth rows in Fig. 6 illustrate enhanced results obtained collaboratively using NLD, BCCR, AOD, and low-light enhancement methods. According to these images, enhancements have severely amplified noise and artifacts in the raw images. Meanwhile, dehazing algorithms may inaccurately estimate the global atmospheric light, so the color of these images severely deviates. We conclude that low-light enhancement algorithms, such as BIMEF, JED, FBE, and LIME, do not favor image quality when collaborating with dehazing algorithms

because the collaborations produce harsh noise and artifact amplifications.

E. PENDING ISSUES

We still have two unsolved problems. First, parameter selection still needs simplifications for the proposed framework, especially for selecting S_r and S_R . The two parameters decide patch sizes in Algorithms 1 and 2; empirically, this depends on the image's length and width. Our dehazing algorithm is mainly based on (22) and can be solved using the box filter [54]; this leads to a time complexity as $O(n)$, where n indicates the number of pixels. The time complexity seems fine; however, the selected patch sizes are the primary factor in determining the execution time. According to our experiment that repeatedly executes the proposed method 100 times, the proposed method takes 2.1 seconds with the help of Nvidia GeForce RTX 2060 to deal with a one-megapixel image. Down-sampling the input to a half-mega-pixel image and using the default setting may be a good solution; this takes only 0.8 seconds. Alternatively, the image pyramid and machine-learning technique may accelerate the proposed framework, too.

The second is related to the adaptation. As discussed previously, the proposed framework does not consider the glow caused by the atmosphere and artificial light sources. The

glow is typical for nighttime images taken under fog or haze environments; however, Figs. 6(s)-6(x) show that dehazing algorithms barely remove or suppress the glow caused by the street light. Therefore, it is not realistic to consider the proposed method a solution to the nighttime image. However, the proposed framework improves brightness and visibility like other cases illustrated in Fig 6.

V. CONCLUSION

We propose a novel image enhancement framework to overcome several visibility issues, which result in unclear image content owing to limited visible distance. Low-visibility images are taken under unideal illumination and usually suffer from under-exposure, noise, and artifacts; moreover, they may be affected by haze, fog, or rain. The proposed framework can enhance luminance, reduce harmful effects resulting from the environment, and raise visibility simultaneously; therefore, it is particularly suitable for hazy images captured under low illumination. The proposed framework implements a double-side enhancement in contrast and brightness based on a new dehazing algorithm to increase the visibility distance of the images. We solve over-enhancement issues and successfully produce quality-enhanced images using a novel thresholding method. Experimental results prove that the performance of the proposed method outperforms many algorithms and their combinations. The proposed framework will favor recognition accuracy when dealing with objects in low-visibility images. Therefore, our future work focuses on accuracy improvements of object recognition tasks.

REFERENCES

- [1] K. He, J. Sun, and X. Tang, "Single image haze removal using dark channel prior," *IEEE Trans. Pattern Anal. Mach. Intell.*, vol. 33, no. 12, pp. 2341–2353, Dec. 2011, doi: [10.1109/TPAMI.2010.168](https://doi.org/10.1109/TPAMI.2010.168).
- [2] G. Meng, Y. Wang, J. Duan, S. Xiang, and C. Pan, "Efficient image dehazing with boundary constraint and contextual regularization," in *Proc. IEEE Int. Conf. Comput. Vis.*, Dec. 2013, pp. 617–624.
- [3] Q. Zhu, J. Mai, and L. Shao, "A fast single image haze removal algorithm using color attenuation prior," *IEEE Trans. Image Process.*, vol. 24, no. 11, pp. 3522–3533, Nov. 2015, doi: [10.1109/TIP.2015.2446191](https://doi.org/10.1109/TIP.2015.2446191).
- [4] D. Berman, T. Treibitz, and S. Avidan, "Non-local image dehazing," in *Proc. IEEE Conf. Comput. Vis. Pattern Recognit. (CVPR)*, Jun. 2016, pp. 1674–1682.
- [5] B. Cai, X. Xu, K. Jia, C. Qing, and D. Tao, "DehazeNet: An end-to-end system for single image haze removal," *IEEE Trans. Image Process.*, vol. 25, no. 11, pp. 5187–5198, Nov. 2016, doi: [10.1109/TIP.2016.2598681](https://doi.org/10.1109/TIP.2016.2598681).
- [6] W. Ren, S. Liu, H. Zhang, J. Pan, X. Cao, and M. Yang, "Single image dehazing via multi-scale convolutional neural networks," in *Proc. Eur. Conf. Comput. Vis. (ECCV)*, Oct. 2016, pp. 154–169.
- [7] B. Li, X. Peng, Z. Wang, J. Xu, and D. Feng, "AOD-Net: All-in-one dehazing network," in *Proc. IEEE Int. Conf. Comput. Vis. (ICCV)*, Oct. 2017, pp. 4780–4788.
- [8] P.-J. Liu, S.-J. Horng, J.-S. Lin, and T. Li, "Contrast in haze removal: Configurable contrast enhancement model based on dark channel prior," *IEEE Trans. Image Process.*, vol. 28, no. 5, pp. 2212–2227, May 2019, doi: [10.1109/TIP.2018.2823424](https://doi.org/10.1109/TIP.2018.2823424).
- [9] W. Ren, L. Ma, J. Zhang, J. Pan, X. Cao, W. Liu, and M.-H. Yang, "Gated fusion network for single image dehazing," in *Proc. IEEE/CVF Conf. Comput. Vis. Pattern Recognit.*, Jun. 2018, pp. 3253–3261.
- [10] D. Yang and J. Sun, "Proximal dehaze-Net: A prior learning-based deep network for single image dehazing," in *Proc. Eur. Conf. Comput. Vis. (ECCV)*, Sep. 2018, pp. 702–717.
- [11] H. Dong, J. Pan, L. Xiang, Z. Hu, X. Zhang, F. Wang, and M.-H. Yang, "Multi-scale boosted dehazing network with dense feature fusion," in *Proc. IEEE/CVF Conf. Comput. Vis. Pattern Recognit. (CVPR)*, Jun. 2020, pp. 2154–2164, doi: [10.1109/CVPR42600.2020.00223](https://doi.org/10.1109/CVPR42600.2020.00223).
- [12] X. Liu, H. Li, and C. Zhu, "Joint contrast enhancement and exposure fusion for real-world image dehazing," *IEEE Trans. Multimedia*, vol. 24, pp. 3934–3946, 2022, doi: [10.1109/TMM.2021.3110483](https://doi.org/10.1109/TMM.2021.3110483).
- [13] B.-H. Chen, S.-C. Huang, C.-Y. Li, and S.-Y. Kuo, "Haze removal using radial basis function networks for visibility restoration applications," *IEEE Trans. Neural Netw. Learn. Syst.*, vol. 29, no. 8, pp. 3828–3838, Aug. 2018, doi: [10.1109/TNNLS.2017.2741975](https://doi.org/10.1109/TNNLS.2017.2741975).
- [14] Z. Wang, A. C. Bovik, H. R. Sheikh, and E. P. Simoncelli, "Image quality assessment: From error visibility to structural similarity," *IEEE Trans. Image Process.*, vol. 13, no. 4, pp. 600–612, Apr. 2004.
- [15] G. Sharma, W. Wu, and E. N. Dalal, "The CIEDE2000 color-difference formula: Implementation notes, supplementary test data, and mathematical observations," *COLOR Res. Appl.*, vol. 30, no. 1, pp. 21–30, Feb. 2005.
- [16] X. Ren, M. Li, W. -H. Cheng, and J. Liu, "Joint enhancement and denoising method via sequential decomposition," in *Proc. IEEE Int. Symp. Circuits Syst. (ISCAS)*, Florence, Italy, May 2018, pp. 1–5, doi: [10.1109/ISCAS.2018.8351427](https://doi.org/10.1109/ISCAS.2018.8351427).
- [17] N. Venkatanath, D. Praneeth, B. M. Chandrasekhar, S. S. Channappayya, and S. S. Medasani, "Blind image quality evaluation using perception based features," in *Proc. 21st Nat. Conf. Commun. (NCC)*, Mar. 2015, pp. 1–6, doi: [10.1109/NCC.2015.7084843](https://doi.org/10.1109/NCC.2015.7084843).
- [18] A. Mittal, A. K. Moorthy, and A. C. Bovik, "No-reference image quality assessment in the spatial domain," *IEEE Trans. Image Process.*, vol. 21, no. 12, pp. 4695–4708, Dec. 2012, doi: [10.1109/TIP.2012.2214050](https://doi.org/10.1109/TIP.2012.2214050).
- [19] A. Mittal, R. Soundararajan, and A. C. Bovik, "Making a 'completely blind' image quality analyzer," *IEEE Signal Process. Lett.*, vol. 20, no. 3, pp. 209–212, Mar. 2013, doi: [10.1109/LSP.2012.2227726](https://doi.org/10.1109/LSP.2012.2227726).
- [20] H. Wang, Y. Chen, Y. Cai, L. Chen, Y. Li, M. A. Sotelo, and Z. Li, "SFNet-N: An improved SFNet algorithm for semantic segmentation of low-light autonomous driving road scenes," *IEEE Trans. Intell. Transp. Syst.*, vol. 23, no. 11, pp. 21405–21417, Nov. 2022, doi: [10.1109/TITS.2022.3177615](https://doi.org/10.1109/TITS.2022.3177615).
- [21] B. Li, W. Ren, D. Fu, D. Tao, D. Feng, W. Zeng, and Z. Wang, "Benchmarking single-image dehazing and beyond," *IEEE Trans. Image Process.*, vol. 28, no. 1, pp. 492–505, Jan. 2019.
- [22] W. Yang, "Advancing image understanding in poor visibility environments: A collective benchmark study," *IEEE Trans. Image Process.*, vol. 29, pp. 5737–5752, 2020, doi: [10.1109/TIP.2020.2981922](https://doi.org/10.1109/TIP.2020.2981922).
- [23] Y. Sumi, B. K. Kim, and M. Kodama, "Evaluation of detection performance for safety-related sensors in low-visibility environments," *IEEE Sensors J.*, vol. 21, no. 17, pp. 18855–18863, Sep. 2021, doi: [10.1109/JSEN.2021.3089207](https://doi.org/10.1109/JSEN.2021.3089207).
- [24] J. Li, F. Wang, K. Xue, and Y. Hao, "Research on machine learning-based nowcasting method for low visibility weather in Urumqi airport," in *Proc. 4th Int. Conf. Adv. Comput. Technol., Inf. Sci. Commun. (CTISC)*, Suzhou, China, Apr. 2022, pp. 1–6, doi: [10.1109/CTISC54888.2022.9849817](https://doi.org/10.1109/CTISC54888.2022.9849817).
- [25] H.-F. Wang, Y.-H. Shan, T. Hao, X.-M. Zhao, S.-Z. Song, H. Huang, and J.-J. Zhang, "Vehicle-road environment perception under low-visibility condition based on polarization features via deep learning," *IEEE Trans. Intell. Transp. Syst.*, vol. 23, no. 10, pp. 17873–17886, Oct. 2022, doi: [10.1109/TITS.2022.3157901](https://doi.org/10.1109/TITS.2022.3157901).
- [26] M. Yang, J. Liu, and Z. Li, "Superpixel-based single nighttime image haze removal," *IEEE Trans. Multimedia*, vol. 20, no. 11, pp. 3008–3018, Nov. 2018, doi: [10.1109/TMM.2018.2820327](https://doi.org/10.1109/TMM.2018.2820327).
- [27] W. Yan, R. T. Tan, and D. Dai, "Nighttime defogging using high-low frequency decomposition and grayscale-color networks," in *Proc. Eur. Conf. Comput. Vis. (ECCV)*, 2020, pp. 473–488.
- [28] Y. Liu, Z. Yan, J. Tan, and Y. Li, "Multi-purpose oriented single nighttime image haze removal based on unified variational retinex model," *IEEE Trans. Circuits Syst. Video Technol.*, vol. 33, no. 4, pp. 1643–1657, Apr. 2023, doi: [10.1109/TCSVT.2022.3214430](https://doi.org/10.1109/TCSVT.2022.3214430).
- [29] Y. Liu, Z. Yan, T. Ye, A. Wu, and Y. Li, "Single nighttime image dehazing based on unified variational decomposition model and multi-scale contrast enhancement," *Eng. Appl. Artif. Intell.*, vol. 116, Nov. 2022, Art. no. 105373.
- [30] Y. Gao, H.-M. Hu, B. Li, Q. Guo, and S. Pu, "Detail preserved single image dehazing algorithm based on airlight refinement," *IEEE Trans. Multimedia*, vol. 21, no. 2, pp. 351–362, Feb. 2019, doi: [10.1109/TMM.2018.2856095](https://doi.org/10.1109/TMM.2018.2856095).

- [31] C. Liu, Q. Zhao, Y. Zhang, and K. Tan, "Runway extraction in low visibility conditions based on sensor fusion method," *IEEE Sensors J.*, vol. 14, no. 6, pp. 1980–1987, Jun. 2014, doi: [10.1109/JSEN.2014.2306911](https://doi.org/10.1109/JSEN.2014.2306911).
- [32] X. Fu, D. Zeng, Y. Huang, Y. Liao, X. Ding, and J. Paisley, "A fusion-based enhancing method for weakly illuminated images," *Signal Process.*, vol. 129, pp. 82–96, Dec. 2016.
- [33] Z. Ying, G. Li, and W. Gao, "A bio-inspired multi-exposure fusion framework for low-light image enhancement," 2017, *arXiv:1711.00591*.
- [34] A. Singh, A. Chougule, P. Narang, V. Chamola, and F. R. Yu, "Low-light image enhancement for UAVs with multi-feature fusion deep neural networks," *IEEE Geosci. Remote Sens. Lett.*, vol. 19, pp. 1–5, 2022, doi: [10.1109/LGRS.2022.3181106](https://doi.org/10.1109/LGRS.2022.3181106).
- [35] X. Guo, Y. Li, and H. Ling, "LIME: Low-light image enhancement via illumination map estimation," *IEEE Trans. Image Process.*, vol. 26, no. 2, pp. 982–993, Feb. 2017, doi: [10.1109/TIP.2016.2639450](https://doi.org/10.1109/TIP.2016.2639450).
- [36] H. A. Gasparyan, S. A. Hovhannisyanyan, S. V. Babayan, and S. S. Agaian, "Iterative retinex-based decomposition framework for low light visibility restoration," *IEEE Access*, vol. 11, pp. 40298–40313, 2023, doi: [10.1109/ACCESS.2023.3269719](https://doi.org/10.1109/ACCESS.2023.3269719).
- [37] W. Wang, X. Wu, X. Yuan, and Z. Gao, "An experiment-based review of low-light image enhancement methods," *IEEE Access*, vol. 8, pp. 87884–87917, 2020.
- [38] M. Veluchamy, A. K. Bhandari, and B. Subramani, "Optimized Bezier curve based intensity mapping scheme for low light image enhancement," *IEEE Trans. Emerg. Topics Comput. Intell.*, vol. 6, no. 3, pp. 602–612, Jun. 2022, doi: [10.1109/TETCI.2021.3053253](https://doi.org/10.1109/TETCI.2021.3053253).
- [39] K. Wei, Y. Fu, Y. Zheng, and J. Yang, "Physics-based noise modeling for extreme low-light photography," *IEEE Trans. Pattern Anal. Mach. Intell.*, vol. 44, no. 11, pp. 8520–8537, Nov. 2022, doi: [10.1109/TPAMI.2021.3103114](https://doi.org/10.1109/TPAMI.2021.3103114).
- [40] S. Mandal and A. N. Rajagopalan, "Local proximity for enhanced visibility in haze," *IEEE Trans. Image Process.*, vol. 29, pp. 2478–2491, 2020, doi: [10.1109/TIP.2019.2957931](https://doi.org/10.1109/TIP.2019.2957931).
- [41] J. Liu, X. Chang, Y. Li, Y. Ji, J. Fu, and J. Zhong, "STCN-Net: A novel multi-feature stream fusion visibility estimation approach," *IEEE Access*, vol. 10, pp. 120329–120342, 2022, doi: [10.1109/ACCESS.2022.3218456](https://doi.org/10.1109/ACCESS.2022.3218456).
- [42] H.-M. Hu, Q. Guo, J. Zheng, H. Wang, and B. Li, "Single image defogging based on illumination decomposition for visual maritime surveillance," *IEEE Trans. Image Process.*, vol. 28, no. 6, pp. 2882–2897, Jun. 2019, doi: [10.1109/TIP.2019.2891901](https://doi.org/10.1109/TIP.2019.2891901).
- [43] H.-M. Hu, H. Zhang, Z. Zhao, B. Li, and J. Zheng, "Adaptive single image dehazing using joint local–global illumination adjustment," *IEEE Trans. Multimedia*, vol. 22, no. 6, pp. 1485–1495, Jun. 2020, doi: [10.1109/TMM.2019.2944260](https://doi.org/10.1109/TMM.2019.2944260).
- [44] C.-Y. Li, J.-C. Guo, R.-M. Cong, Y.-W. Pang, and B. Wang, "Underwater image enhancement by dehazing with minimum information loss and histogram distribution prior," *IEEE Trans. Image Process.*, vol. 25, no. 12, pp. 5664–5677, Dec. 2016, doi: [10.1109/TIP.2016.2612882](https://doi.org/10.1109/TIP.2016.2612882).
- [45] H. Li, Q. Wu, K. N. Ngan, H. Li, Meng, and Fanman, "Single image dehazing via region adaptive two-shot network," *IEEE Multimedia Mag.*, vol. 28, no. 3, pp. 97–106, Jul. 2021, doi: [10.1109/MMUL.2021.3052821](https://doi.org/10.1109/MMUL.2021.3052821).
- [46] X. Shen, C. Zhou, L. Xu, and J. Jia, "Mutual-structure for joint filtering," in *Proc. IEEE Int. Conf. Comput. Vis. (ICCV)*, Dec. 2015, pp. 3406–3414.
- [47] K. He, J. Sun, and X. Tang, "Guided image filtering," *IEEE Trans. Pattern Anal. Mach. Intell.*, vol. 35, no. 6, pp. 1397–1409, Jun. 2013, doi: [10.1109/TPAMI.2012.213](https://doi.org/10.1109/TPAMI.2012.213).
- [48] L. Zhang, A. Zhu, S. Zhao, and Y. Zhou, "Simulation of atmospheric visibility impairment," *IEEE Trans. Image Process.*, vol. 30, pp. 8713–8726, 2021, doi: [10.1109/TIP.2021.3120044](https://doi.org/10.1109/TIP.2021.3120044).
- [49] S. A. Mastani and K. Shilpa, "New approach of estimating PSNR-B for de-blocked images," 2013, *arXiv:1306.5293*.
- [50] H. Z. Nafchi, A. Shahkolaei, R. F. Moghaddam, and M. Cheriet, "FSITM: A feature similarity index for tone-mapped images," *IEEE Signal Process. Lett.*, vol. 22, no. 8, pp. 1026–1029, Aug. 2015, doi: [10.1109/LSP.2014.2381458](https://doi.org/10.1109/LSP.2014.2381458).
- [51] H. Yeganeh and Z. Wang, "Objective quality assessment of tone-mapped images," *IEEE Trans. Image Process.*, vol. 22, no. 2, pp. 657–667, Feb. 2013.
- [52] X. Min, G. Zhai, K. Gu, Y. Zhu, J. Zhou, G. Guo, X. Yang, X. Guan, and W. Zhang, "Quality evaluation of image dehazing methods using synthetic hazy images," *IEEE Trans. Multimedia*, vol. 21, no. 9, pp. 2319–2333, Sep. 2019, doi: [10.1109/TMM.2019.2902097](https://doi.org/10.1109/TMM.2019.2902097).
- [53] Y. Zhang, L. Ding, and G. Sharma, "HazeRD: An outdoor scene dataset and benchmark for single image dehazing," in *Proc. IEEE Int. Conf. Image Process. (ICIP)*, Sep. 2017, pp. 3205–3209.
- [54] M. Nakamura and N. Fukushima, *Fast Implementation of Box Filtering*. Nagoya, Japan: Nagoya Institute of Technology, 2017. [Online]. Available: https://fukushima.web.nitech.ac.jp/paper/2017_iwait_nakamura.pdf



PING JUEI LIU received the Ph.D. degree in computer science and information engineering from the National Taiwan University of Science and Technology. He is currently an Assistant Professor with the Department of Artificial Intelligence and Computer Engineering, National Chin-Yi University of Technology, Taiwan. His research interests include computational photography, image processing, and machine learning.

• • •